Proceedings of the Seventh International Conference on
Railway Technology: Research, Development and Maintenance
Edited by: J. Pombo
Civil-Comp Conferences, Volume 15, Paper 11.5
Civil-Comp Press, Edinburgh, United Kingdom, 2026
ISSN: 2753-3239, doi: 10.4203/ccc.15.11.5

Parameter Model of Long Stator Linear Motor Based on Dynamic Differential Permeability and Equivalent Air Gap

R. Gao[1,2], Q. Ge[1,2], L. Zhao[1,2], J. Zhu[1] and B. Zhang[1,2]

[1]State Key Laboratory of High Density Electromagnetic Power and Systems, Institute of Electrical Engineering, China
[2]University of Chinese Academy of Sciences, Beijing, China

Abstract

The conventional electromagnetic suspension (EMS) maglev motor is operated under conditions characterized by pronounced air-gap fluctuations and magnetic saturation, which significantly degrade motor parameter accuracy and controllability. Conventional magnetic-circuit-based parameter models generally neglect saturation effects and thus exhibit considerable deviations from actual operating characteristics. In this paper, a parameter model of long stator linear motor based on dynamic differential permeability and equivalent air gap is proposed by combining analytical model with finite element analysis. An equivalent air-gap model incorporating iron-core reluctance is first derived based on the magnetic circuit method. Subsequently, finite element simulations are performed to obtain magnetic field intensity data in both the air gap and the iron core, and a dynamic magnetization characterization approach based on differential permeability is adopted to identify the saturation-dependent relative permeability of the core material. Finally, a saturation-aware analytical parameter model is established by integrating the equivalent air gap with the identified permeability characteristics. Comparative analyses with finite element results demonstrate that the proposed method significantly improves parameter prediction accuracy under small air-gap and magnetic saturation conditions, thereby providing a reliable foundation for high-performance traction and levitation control of EMS maglev systems.

Keywords: high-speed maglev, long stator linear synchronous motor, magnetic saturation, air gap relative permeance, motor parameters, finite element simulation.

1 Introduction

When an electromagnetic suspension (EMS) high-speed maglev train operates under scenarios such as open-line sections, tunnels, strong crosswind conditions, and train passing events, significant aerodynamic drag, lift, and transient pressure loads are induced. The resulting coupled aerodynamic effects act on high-speed multi-car trainsets, generating rolling and pitching moments, which aggravate dynamic fluctuations of the levitation air gap[1][3]. From a control perspective, such air-gap variations directly influence electromagnetic force generation and motor parameter stability, thereby imposing stringent requirements on the accuracy and robustness of control-oriented motor models.

Moreover, track irregularities caused by environmental temperature variations, pier settlement, and curved alignments, together with the increased inherent air-gap fluctuations associated with train speeds up to 600 km/h, give rise to operating conditions characterized by locally reduced air gaps and magnetic saturation. Under these conditions, motor parameter models derived from conventional magnetic circuit assumptions deviate significantly from actual operating characteristics. Consequently, traction and levitation control strategies that rely on fixed or pre-identified parameters experience performance degradation, leading to thrust force oscillations of the linear synchronous motor. These force fluctuations are directly transmitted to the vehicle body, inducing vibrations and deteriorating ride comfort[4].

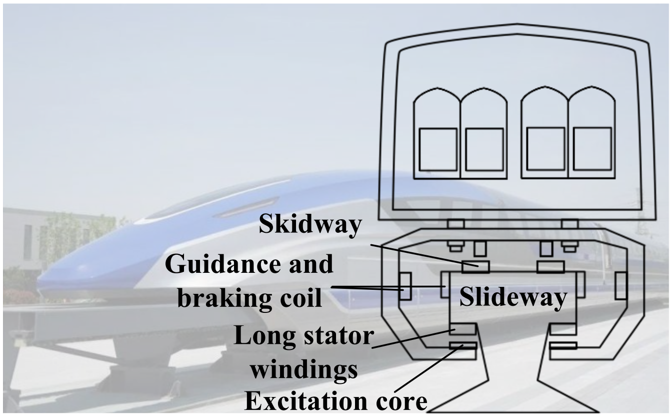

Figure 1： Connection diagram of three-step power supply switching method.

For conventional EMS maglev motors, finite element analysis (FEA) and analytical modeling are the two primary approaches used for parameter identification. FEA[5] enables accurate consideration of slotting effects, core nonlinearity, and end effects, and thus provides high-fidelity electromagnetic characteristics. However, FEA-based models are generally unsuitable for real-time control applications due to their high computational burden and the lack of explicit analytical expressions for key control-relevant parameters, such as inductance and force coefficients. As a result, their direct applicability in control system design, stability analysis, and online parameter adaptation remains limited.

Analytical methods, including the magnetic circuit method, subdomain method, equivalent magnetic network method, winding function method, and space harmonic method, are more amenable to control-oriented modeling. Among them, the magnetic circuit method[6] provides parameters with clear physical interpretation and facilitates controller implementation. Nevertheless, the time-varying air gap and complex magnetic flux paths of EMS maglev motors, particularly under levitation gap fluctuations, make accurate magnetic circuit construction highly dependent on empirical assumptions. This limitation leads to insufficient accuracy in magnetic field and parameter estimation, especially under magnetic saturation conditions. In addition, the nonperiodic magnetic field distribution caused by unequal pole pitch designs and salient-pole structures in long stator linear synchronous motor (LSLSM) increases the modeling complexity of subdomain[7] and equivalent magnetic network methods[8] while both subdomain and winding function methods[9] exhibit inherent difficulties in capturing saturation-dependent parameter variations.

To address the conflict between modeling accuracy and control applicability, hybrid modeling approaches that combine analytical formulations with finite element data have recently attracted increasing attention. Motivated by the above considerations, this paper proposes a parameter model of long stator linear motor based on dynamic differential permeability and equivalent air gap. The proposed model provides accurate inductance and force-related parameters over a wide operating range, thereby improving parameter consistency and controllability. Comparative analyses demonstrate that the proposed approach significantly enhances modeling accuracy while maintaining suitability for control system design and implementation.

2 Time-Varying Characteristics of Motor Parameters During the Changeover Process of LS-LSM

2.1 Establishment of the Air-Gap Permeance Function of the Conventional EMS Maglev Motor

The main parameters of the long-stator and excitation magnetic pole of the conventional EMS maglev motor [10] are listed in Tab. 1.

Tab. 1 Main parameters of EMS motor

symbol	parameter	value
τ_s	stator pole pitch (mm)	258
τ_N	stator slot pitch (mm)	86
b_N	stator slot width (mm)	43
b_e	stator core thickness (mm)	185
N_s	number of turns of stator winding (turns)	1
τ_m	excitation pole pitch (mm)	266.5
b_m	excitation pole width (mm)	166.5
b_f	excitation pole core thickness (mm)	170
N_m	number of turns of excitation winding (turns)	270
l_{air}	rated levitation height (mm)	10
l_s	air-gap height at stator slot depth (mm)	41
l_m	air-gap height at excitation core slot depth (mm)	120

Due to the deep slot geometry of the long-stator linear synchronous motor windings, the air gap between the stator core and the excitation core cannot be regarded as constant. Therefore, an air-gap permeance function is introduced to characterize the influence of slotting effects on the air-gap magnetic field [11].

According to the relative displacement x_s between the centerline of phase-A stator teeth and the centerline of the excitation magnetic pole, the air-gap length function can be classified into five categories. One representative case corresponding to a relatively small displacement is illustrated in Fig. 2, in which the air-gap length function is divided into nine segments.

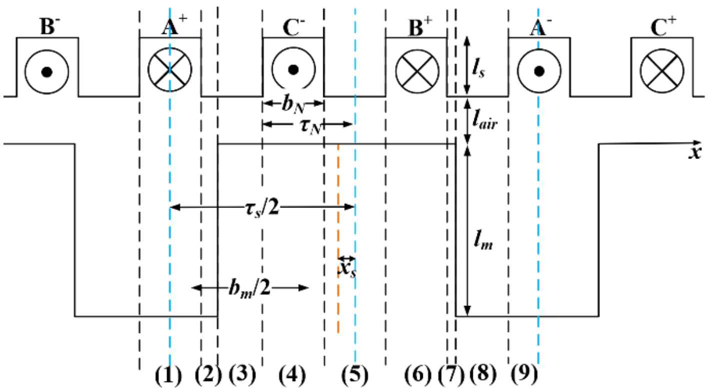

Fig.2 Diagram of the stator with a small relative displacement to the excitation central axis

$$
\begin{cases}
-\frac{\tau_s}{2}-x_s < x \le -\frac{\tau_s}{2}+\frac{b_N}{2}-x_s & l_{air}+l_s+l_{\mathrm{m}} \\
-\frac{\tau_s}{2}+\frac{b_N}{2}-x_s < x \le -\frac{b_m}{2} & l_{air}+l_m \\
-\frac{b_m}{2} < x \le -\frac{\tau_N}{2}-\frac{b_N}{2}-x_s & l_{air} \\
-\frac{\tau_N}{2}-\frac{b_N}{2}-x_s < x \le -\frac{\tau_N}{2}+\frac{b_N}{2}-x_s & l_{air}+l_s \\
-\frac{\tau_N}{2}+\frac{b_N}{2}-x_s < x \le \frac{\tau_N}{2}-\frac{b_N}{2}-x_s & l_{air} \\
\frac{\tau_N}{2}-\frac{b_N}{2}-x_s < x \le \frac{\tau_N}{2}+\frac{b_N}{2}-x_s & l_{air}+l_s \\
\frac{\tau_N}{2}+\frac{b_N}{2}-x_s < x \le \frac{b_m}{2} & l_{air} \\
\frac{b_m}{2} < x \le \frac{\tau_s}{2}-\frac{b_N}{2}-x_s & l_{air}+l_{\mathrm{m}} \\
\frac{\tau_s}{2}-\frac{b_N}{2}-x_s < x \le \frac{\tau_s}{2}-x_s & l_{air}+l_s+l_{\mathrm{m}}
\end{cases}
\quad (1)
$$

where x denotes the coordinate defined on the excitation core; x_s represents the relative displacement between the centerline of the stator phase-A winding and the centerline of the excitation magnetic pole. A positive value of x_s indicates a leftward displacement of the stator.

The air-gap permeance function $\lambda(x,x_s)$ is expressed in a Fourier series, and the terms varying with x_s are rearranged as

$$\lambda=\lambda_0+\sum_n\frac{1}{2n}\begin{bmatrix} a_1\cos\left(\frac{2n\pi}{\tau_s}(x+x_s)\right)+a_2\cos\left(\frac{2n\pi}{\tau_s}x\right) \\ +b_1\sin\left(\frac{2n\pi}{\tau_s}(x+x_s)\right)+b_2\sin\left(\frac{2n\pi}{\tau_s}x\right)\end{bmatrix} \tag{2}$$

where λ_0 denotes the average air-gap permeance. The coefficients a_1 and $b_1$correspond to the Fourier coefficients of the n-th harmonic components that vary with x_s, while a_2 and b_2 represent the coefficients of the harmonic components independent of x_s.

The coefficients of the air-gap permeance function corresponding to the stator–rotor relative displacement described by (1) are given as

$$\begin{cases} \lambda_0=\frac{\mu_0}{2\tau_s}\begin{bmatrix}\frac{b_N}{l_{air}+l_s+l_{\mathrm{m}}}+\frac{2b_N}{l_{air}+l_s} \\ +\frac{\tau_s-b_N-b_m}{l_{air}+l_m}+\frac{b_m-2b_N}{l_{air}}\end{bmatrix} \\ a_1=\frac{4\mu_0}{\pi}\begin{bmatrix}\left(\frac{1}{l_{air}}-\frac{1}{l_{air}+l_s}\right)E+ \\ \left(\frac{1}{l_{air}+l_{\mathrm{m}}}-\frac{1}{l_{air}+l_s+l_{\mathrm{m}}}\right)F\end{bmatrix} \\ a_2=\frac{4\mu_0}{\pi}\left(\frac{1}{l_{air}}-\frac{1}{l_{air}+l_m}\right)\sin\left(\frac{n\pi b_m}{\tau_s}\right) \\ b_1=b_2=0 \\ E=\sin\left(\frac{2n\pi}{\tau_s}\frac{\tau_N-b_N}{2}\right)-\sin\left(\frac{2n\pi}{\tau_s}\frac{\tau_N+b_N}{2}\right) \\ F=\sin\left(\frac{2n\pi}{\tau_s}\frac{\tau_s-b_N}{2}\right)\end{cases} \tag{3}$$

where μ_0 is the permeability of free space.

2.2 Air-Gap Magnetomotive Force of the Windings

The actual stator winding current is equivalently represented by a uniformly distributed current sheet along the stator slot width. The resulting air-gap magnetomotive force can be described by a trapezoidal waveform as

$$
\begin{cases}
-\tau_s < x < -\dfrac{\tau_s + b_N}{2} & -F \\
-\dfrac{\tau_s + b_N}{2} < x < -\dfrac{\tau_s - b_N}{2} & -F + \left(x + \dfrac{\tau_s + b_N}{2} \right) \times \dfrac{2F}{b_N} \\
-\dfrac{\tau_s - b_N}{2} < x < \dfrac{\tau_s - b_N}{2} & F \\
\dfrac{\tau_s - b_N}{2} < x < \dfrac{\tau_s + b_N}{2} & F - \left(x - \dfrac{\tau_s - b_N}{2} \right) \times \dfrac{2F}{b_N} \\
\dfrac{\tau_s + b_N}{2} < x < \tau_s & -F
\end{cases}
\tag{4}
$$

where F denotes the amplitude of the air-gap MMF generated by the stator current at an arbitrary instant.

By performing Fourier decomposition on the trapezoidal waveform in (4), the air-gap MMF can be expressed as

$$
\begin{cases}
f_{sa} = \dfrac{8F_a}{\pi^2} \dfrac{\tau_s}{b_N} \displaystyle\sum_{k=1}^{\infty} T \cos\left(\dfrac{(2k-1)\pi}{\tau_s} (x + x_s) \right) \\
f_{sb} = \dfrac{8F_b}{\pi^2} \dfrac{\tau_s}{b_N} \displaystyle\sum_{k=1}^{\infty} T \cos\left(\dfrac{(2k-1)\pi}{\tau_s} (x + x_s - 2\tau_N) \right) \\
f_{sc} = \dfrac{8F_c}{\pi^2} \dfrac{\tau_s}{b_N} \displaystyle\sum_{k=1}^{\infty} T \cos\left(\dfrac{(2k-1)\pi}{\tau_s} (x + x_s + 2\tau_N) \right) \\
T = \dfrac{1}{(2k-1)^2} \cos\left(\dfrac{(2k-1)\pi}{2} \dfrac{\tau_s - b_N}{\tau_s} \right)
\end{cases}
\tag{5}
$$

where F_a, F_b and F_c denote the air-gap MMF amplitudes produced by the three-phase currents at an arbitrary instant; $F_a = N_s I_s \cos(\omega t)$; $F_b = N_s I_s \cos(\omega t - 2\pi/3)$; $F_c = N_s I_s \cos(\omega t + 2\pi/3)$; I_s is the stator current amplitude and ω is the electrical angular frequency of the stator current.

Similarly, the air-gap magnetomotive force generated by the excitation winding current can be expressed as

$$
f_m = \frac{8N_m I_m \tau_m}{\pi^2(\tau_m - b_m)} \sum_{k=1}^{\infty} \frac{\cos\left(\frac{(2k-1)\pi b_m}{2\tau_m}\right) \cos\left(\frac{(2k-1)\pi x}{\tau_s}\right)}{(2k-1)^2}
\tag{6}
$$

where I_m denotes the excitation current.

2.3 Calculation of Inductance Parameters

The expression of the self-inductance of stator phase A is given as

$$
L_A = \frac{\psi_A}{i_A} = \frac{N_s b_e \int_{-\frac{\tau_s}{2} - x_s}^{\frac{\tau_s}{2} - x_s} f_{sa} \lambda(x, x_s) dx}{i_s \cos \omega t}
\tag{7}
$$

The expression of the mutual inductance between stator phase A and the excitation winding is given as

$$M_{AM} = \frac{\psi_{AM}}{i_m} = \frac{N_s b_e \int_{-\frac{\tau_s}{2} - x_s}^{\frac{\tau_s}{2} - x_s} f_m \lambda(x, x_s) dx}{i_m} \tag{8}$$

By substituting (2), (5) and (6) into (7)(8), the expressions of the stator phase-A self-inductance and the mutual inductance between stator phase A and the excitation winding corresponding to one suspension unit (with eight pairs of excitation magnetic poles) are obtained as

$$L_A = L_{s0} \left\{ \begin{array}{l} \sum_{v=1}^{\infty} (-1)^{v+1} M \\ + \sum_{n=1}^{\infty} \sum_{v=1}^{\infty} N\, (-1)^{n-v} \left[\frac{1}{(2n-2v+1)} - \frac{1}{(2n+2v-1)} \right] \left[a_1 \cos\left(-\frac{2n\pi}{\tau_s} \Delta\tau_N \right) - b_1 \sin\left(-\frac{2n\pi}{\tau_s} \Delta\tau_N \right) \right] \\ + \sum_{n=1}^{\infty} \sum_{v=1}^{\infty} N\, (-1)^{n-v} \left[\frac{1}{(2n-2v+1)} - \frac{1}{(2n+2v-1)} \right] \left[a_2 \cos\left(\frac{2n\pi}{\tau_s} x_s \right) - b_2 \sin\left(\frac{2n\pi}{\tau_s} x_s \right) \right] \end{array} \right\}$$

$$M_{AM} = M_{sm0} \left\{ \begin{array}{l} 2\lambda_0 \sum_{v=1}^{\infty} (-1)^{v-1} G \cos\left(\frac{2v-1}{\tau_m} \pi x_{s0} \right) \\ + \sum_{v=1}^{\infty} \sum_{n=1}^{\infty} a_1 H\, (-1)^{n-v} \left[\frac{\cos\left(-\frac{2n}{\tau_s} \pi \Delta\tau_N - \frac{2v-1}{\tau_m} \pi x_{s0} \right)}{2n-2v+1} - \frac{\cos\left(-\frac{2n}{\tau_s} \pi \Delta\tau_N + \frac{2v-1}{\tau_m} \pi x_{s0} \right)}{2n+2v-1} \right] \\ + \sum_{v=1}^{\infty} \sum_{n=1}^{\infty} a_2 H\, (-1)^{n-v} \left[\frac{\cos\left(\frac{2n-2v+1}{\tau_s} \pi x_{s0} \right)}{2n-2v+1} - \frac{\cos\left(\frac{2n+2v-1}{\tau_s} \pi x_{s0} \right)}{2n+2v-1} \right] \\ - \sum_{v=1}^{\infty} \sum_{n=1}^{\infty} b_1 H (-1)^{n-v} \left[\frac{\sin\left(-\frac{2n}{\tau_s} \pi \Delta\tau_N - \frac{2v-1}{\tau_m} \pi x_{s0} \right)}{2n-2v+1} - \frac{\sin\left(-\frac{2n}{\tau_s} \pi \Delta\tau_N + \frac{2v-1}{\tau_m} \pi x_{s0} \right)}{2n+2v-1} \right] \\ - \sum_{v=1}^{\infty} \sum_{n=1}^{\infty} b_2 H (-1)^{n-v} \left[\frac{\sin\left(\frac{2n-2v+1}{\tau_m} \pi x_{s0} \right)}{2n-2v+1} - \frac{\sin\left(\frac{2n+2v-1}{\tau_m} \pi x_{s0} \right)}{2n+2v-1} \right] \end{array} \right\} \tag{9}$$

where L_{s0}, M, and N are the coefficients used for calculating the stator winding inductance, and M_{sm0}, G, and H are the coefficients used for calculating the mutual inductance between the stator and excitation windings. P denotes the number of pole pairs of the motor, while n and v represent the harmonic orders in the Fourier decomposition. Their specific expressions are given as

$$\begin{array}{l} L_{s0} = \frac{8PN_s^2 b_e \tau_s^2}{\pi^3 b_N}, M = \frac{2\lambda_0}{(2v-1)^3} \cos\left(\frac{(2v-1)\pi}{2} \frac{\tau_s - b_N}{\tau_s} \right),\ N = \frac{1}{2n} \frac{1}{(2v-1)^2} \cos\left(\frac{(2v-1)\pi}{2} \frac{\tau_s - b_N}{\tau_s} \right) \\ M_{sm0} = \frac{8PN_s N_m b_e \tau_m^2}{\pi^3 (\tau_m - b_m)},\ G = \frac{1}{(2v-1)^3} \cos\left(\frac{(2v-1)\pi}{2} \frac{b_m}{\tau_m} \right),\ H = \frac{1}{2n} \frac{1}{(2v-1)^2} \cos\left(\frac{(2v-1)\pi}{2} \frac{b_m}{\tau_m} \right) \end{array} \tag{10}$$

3 Motor Parameter Model Considering Magnetic Saturation

3.1 Equivalent Air-Gap Calculation

When the iron core enters magnetic saturation, the magnetic reluctance of the core can no longer be neglected. Under the ideal sinusoidal assumption, the magnetic field distributions in the air gap and the iron core are illustrated in Fig. 4.

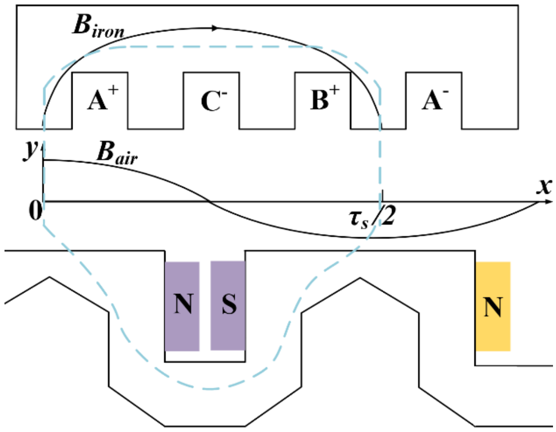

Fig. 3 Diagram of magnetic field distribution in the motor core and air gap

Under this ideal sinusoidal condition, the magnetic field distributions in the air gap and the iron core can be concisely expressed as

$$\begin{cases} B_{air} = B_1 \cos(\dfrac{\pi}{\tau_s} x) \\ B_{iron} = B_2 \sin(\dfrac{\pi}{\tau_s} x) \end{cases} \tag{11}$$

where B_{air} denotes the magnetic flux density in the air gap, B_{iron} denotes the magnetic flux density in the iron core, B_1 represents the peak value of the magnetic flux density in the air gap, and B_2 represents the peak value of the magnetic flux density in the iron core.

Since the magnetic flux in the air gap is equal to the magnetic flux entering the iron core cross section, the following relationship holds:

$$\begin{cases} \varphi_{air} = b_e \displaystyle\int_0^{\frac{\tau_m}{2}} B_1 \cos(\dfrac{\pi}{\tau_s} x) dx \\ \varphi_{iron} = b_e \displaystyle\int_0^{\frac{\tau_m}{2}} B_2 \sin(\dfrac{\pi}{\tau_s} x) dx \\ \varphi_{air} = \varphi_{iron} \end{cases} \tag{12}$$

where φ_{air} denotes the magnetic flux in the air gap and φ_{iron} denotes the magnetic flux in the iron core.

From (12), the relationship between B_1 and B_2 can be derived as

$$B_2 = \frac{B_1 \sin\left(\dfrac{\pi}{\tau_s} \dfrac{\tau_m}{2}\right)}{1 - \cos\left(\dfrac{\pi}{\tau_s} \dfrac{\tau_m}{2}\right)} \tag{13}$$

The magnetic pressure drop along half of the magnetic path indicated by the dashed line in Fig. 4 is expressed as

$$U_M^{'} = \int_l H dl = \frac{B_1}{\mu_0} l_{air} + 2 \frac{B_2}{\mu_0 \mu_r} \frac{\tau_s}{\pi} \tag{14}$$

where μ_r denotes the relative permeability of the iron core material.

By substituting (13) into (14), the following expression is obtained:

$$U_M^{'} = \frac{B_1}{\mu_0} l_{air} \left[1 + \frac{\tau_s}{2\pi\mu_r l_{air}} \frac{\sin\left(\frac{\pi}{\tau_s}\frac{\tau_m}{2}\right)}{1-\cos\left(\frac{\pi}{\tau_s}\frac{\tau_m}{2}\right)} \right] \tag{15}$$

When magnetic saturation of the iron core is not considered, the magnetic pressure drop of the motor U_M is given by

$$U_M = \frac{B_1}{\mu_0} l_{air} \tag{16}$$

Based on (20) and (21), the equivalent air gap *l'_air* can be derived as

$$l_{air}^{'} = l_{air} \left[1 + \frac{\tau_s}{2\pi\mu_r l_{air}} \frac{\sin\left(\frac{\pi}{\tau_s}\frac{\tau_m}{2}\right)}{1-\cos\left(\frac{\pi}{\tau_s}\frac{\tau_m}{2}\right)} \right] \tag{17}$$

3.2 Dynamic Characterization of Magnetization Effects Based on Differential Permeability

Conventional simplification methods for magnetization curves divide the curve into three regions: the linear region, transition region, and deep saturation region[12]. However, such simplifications neglect the variation of permeability at different continuous points within the transition and deep saturation regions.

To improve the accuracy of dynamic magnetization effect characterization, a differential-permeability-based representation method is adopted, as illustrated in Fig. 4 and expressed in (23). By matching this formulation with finite element magnetic field intensity data, high-precision relative permeability values of the iron core material under different levitation heights can be obtained, as listed in Tab. 2.

$$\mu_r = \frac{1}{\mu_0}\frac{dB}{dH} \tag{18}$$

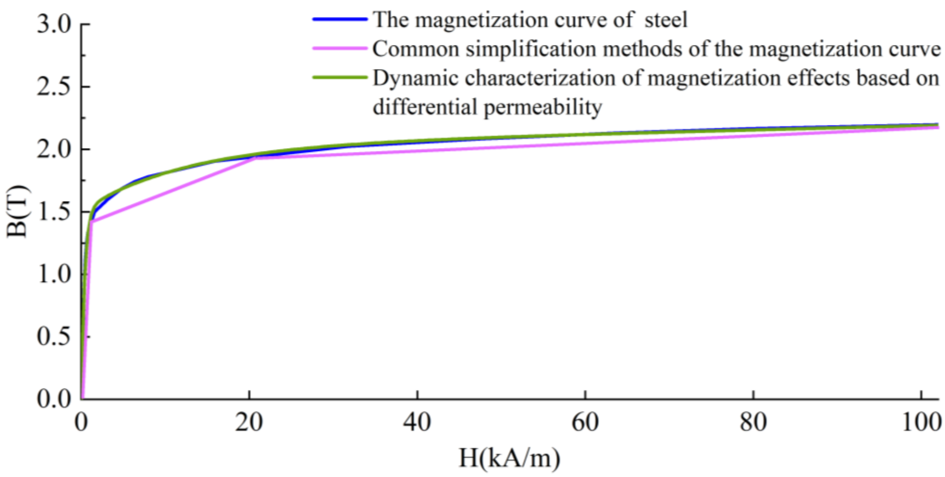

Fig. 4 Alternative methods of expressing magnetization effect

Tab.2 μ_r of iron core at different suspension heights

l_{air}(mm)	μ_r	l_{air}(mm)	μ_r
1	6.01	11	924.16
2	10.65	12	1037.81
3	15.41	13	1121.34
4	21.55	14	1233.74
5	25.94	15	1310.31
6	39.37	16	1336.81
7	142.04	17	1466.57
8	374.68	18	1435.90
9	595.27	19	1459.80
10	755.22		

3.3 Inductance Parameters Considering Magnetic Saturation

The relative permeability μ_r listed in Tab.2 is incorporated into the equivalent air gap l'_{air} in (17). Subsequently, the modified equivalent air gap l'_{air} is substituted into the coefficients of (3), enabling the calculation of inductance parameters that explicitly account for magnetic saturation.

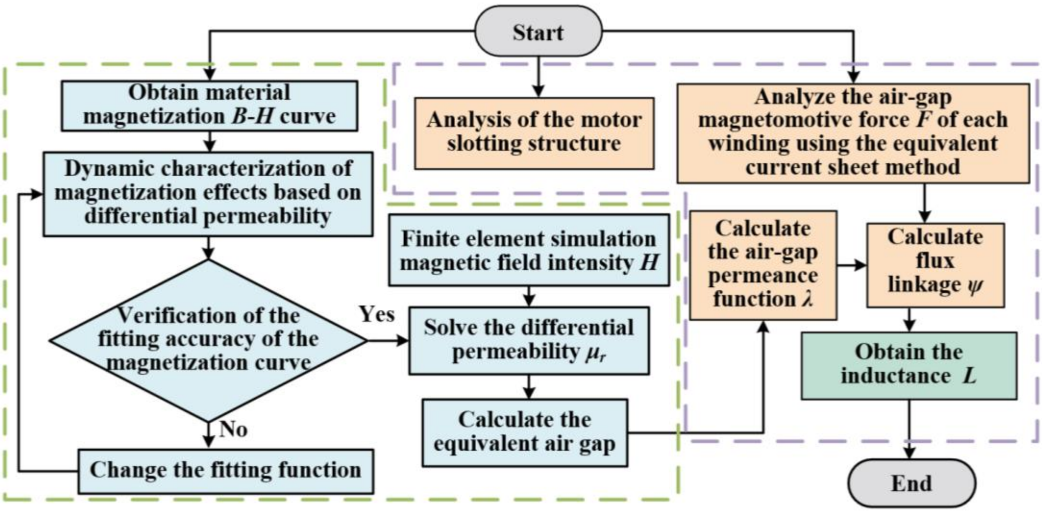

Fig. 5 Flowchart of parameter model considering magnetic saturation

4 Model Validation and Parameter Accuracy Analysis

To verify the accuracy of the proposed analytical approach, the analytical expressions of the inductance parameters derived in Sections 2 and 3 are evaluated using Matlab to obtain their analytical solutions. The resulting values are then compared with those obtained from finite element simulations conducted using Ansys Maxwell.

4.1 Validation of Stator Winding Self-Inductance

Taking the self-inductance of stator phase A as an example, a comparison between the finite element results and the two parameter models is illustrated in Fig. 6. At a levitation height of 5 mm, the relative error between the simulation results and the parameter model that neglects magnetic saturation reaches as high as 75.01%, indicating severe distortion and poor accuracy. In contrast, the proposed saturation-aware parameter model significantly improves the prediction accuracy by 39.43%, demonstrating its effectiveness in capturing saturation effects.

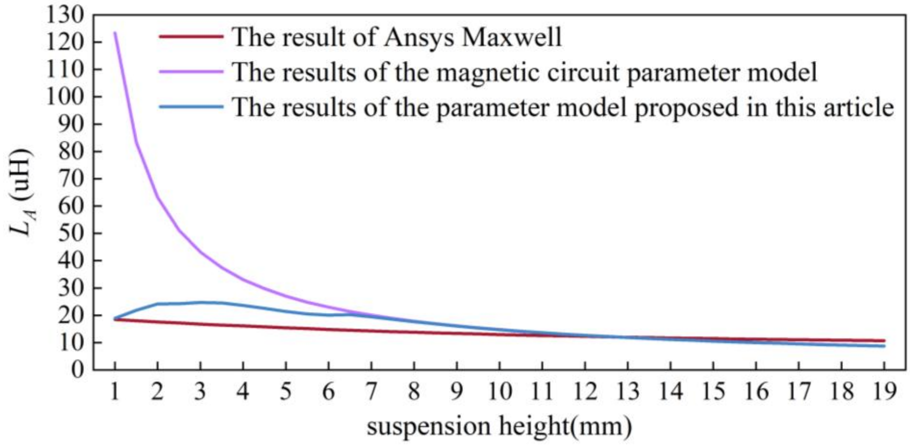

Fig. 6 Comparison of self-inductance for stator phase A

4.2 Validation of Mutual Inductance Between Stator and Excitation Windings

The mutual inductance between stator phase A and the excitation winding is taken as another validation case. The comparison results between the finite element model and the two parameter models are shown in Fig. 7. At a levitation height of 5 mm, the relative error of the parameter model without considering magnetic saturation reaches 46.36%, indicating a substantial deviation from the finite element results. By incorporating magnetic saturation effects, the proposed improved parameter model achieves a significant accuracy improvement of 30.14%.

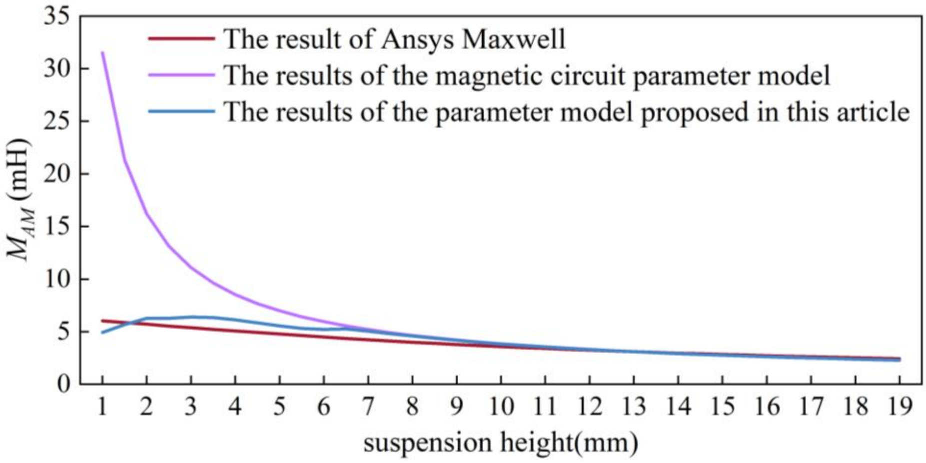

Fig.7 Comparison of stator A phase and excitation mutual inductance

6 Conclusion

In this paper, a control-oriented parameter modeling method for conventional EMS maglev motors considering magnetic saturation has been presented. By introducing an equivalent air-gap model that incorporates iron-core reluctance, the limitations of conventional magnetic circuit methods under saturation conditions are effectively addressed. A differential-permeability-based dynamic magnetization characterization approach is further employed to accurately capture the nonlinear magnetic properties of the core material using finite element field data. On this basis, a saturation-aware analytical inductance parameter model is established.

Comparative results with finite element simulations demonstrate that the proposed model significantly improves the accuracy of both stator self-inductance and stator–excitation mutual inductance predictions, especially under small levitation gap conditions where magnetic saturation is pronounced. The improved parameter fidelity enhances the consistency between analytical models and actual motor behavior, thereby providing a solid foundation for robust traction and levitation control design. The proposed modeling approach achieves a favorable balance between accuracy and control app

Acknowledgements

This work was supported by the National Key Research and Development Program of China (Grant No. 2023YFB4302501-02) and the National Natural Science Foundation of China (Grant No. 52302458).

References

[1] M. Yang, S. Zhong, L. Zhang, et al. “600 km/h moving model rig for high-speed train aerodynamics,” Journal of Wind Engineering and Industrial Aerodynamics, 2022, 227: 105063.

[2] L. Zhang,Y. Gao,T. Lin, et al. “Comparative analysis of crosswind influence on aerodynamic characteristics of superconducting and normal-conducting high-speed maglev trains,” Journal of Wind Engineering and Industrial Aerodynamics, 2025, 265:106182.

[3] M. Ouyang, S. Chen, Q. Li, et al. “Numerical investigation on aerodynamic forces and flow patterns of high-speed trains from open air into long tunnel,” Journal of Wind Engineering and Industrial Aerodynamics, 2022, 229: 105142.

[4] J. Zhu, X. Cao, Q. Ge, et al. "Adaptive-SMO-Based Traction Force Fluctuation Suppression Strategy Considering Suspension System for High-Speed Maglev Train," in *IEEE Transactions on Industrial Electronics*, vol. 71, no. 3, pp. 2289-2299, March 2024.

[5] G. Lv, L. Cui and R. Zhi, "Inductance Analysis of Transverse Flux Linear Synchronous Motor for Maglev Trains Considering Three-Dimensional Operating Conditions," in IEEE Transactions on Industrial Electronics, vol. 71, no. 1, pp. 769-776, Jan. 2024.

[6] H. Wang, J. Zhao, Y. Xiong and H. Xu, "Exact Air Gap Magnetic Field Calculation of a Short Primary Single-Sided Linear Induction Motor Considering Coupling Effects of Slot Harmonics and Longitudinal Dynamic End Effect," in IEEE Transactions on Magnetics, vol. 61, no. 11, pp. 1-12, Nov. 2025.

[7] J. Liu, X. Wang, X. Li, B. Yan, L. Xiong and X. Zhang, "Electromagnetic and Stress Performance Analysis for Synchronous Reluctance Motor Using a New Hybrid Subdomain Method," in IEEE Transactions on Industrial Electronics, vol. 71, no. 8, pp. 8548-8559, Aug. 2024.

[8] X. Zhu, G. Qi, M. Cheng, W. Qin, Y. Liu and J. Huang, "Equivalent Magnetic Network Model of Electrical Machine Based on Three Elements: Magnetic Flux Source, Reluctance, and Magductance," in IEEE Transactions on Transportation Electrification, vol. 11, no. 1, pp. 3538-3548, Feb. 2025.

[9] U. Ayhan and H. Gurleyen, "Advanced Modeling of a 12/10 Variable Flux Reluctance Machine Using Winding and Air-Gap Permeance Functions Considering Saturation and Skew Effects," in IEEE Transactions on Transportation Electrification, vol. 11, no. 4, pp. 10001-10011, Aug. 2025.

[10] J. Cao, X. Deng, D. Li and B. Jia, "Electromagnetic Analysis and Optimization of High-speed Maglev Linear Synchronous Motor Based on Field-circuit Coupling," in CES Transactions on Electrical Machines and Systems, vol. 6, no. 2, pp. 118-123, June 2022.

[11] C. Ma, et al. "3-D Analytical Model of Armature Reaction Field of IPMSM With Multi-Segmented Skewed Poles and Multi-Layered Flat Wire Winding Considering Current Harmonics," in IEEE Access, vol. 8, pp. 151116-151124, 2020.

[12] M. -D. Nguyen, J. -W. Yang, D. -T. Hoang, K. -H. Shin and J. -Y. Choi, "Electromagnetic Analysis of YASA Axial Flux Motor Using Harmonic Modeling Considering Non-Linear Core Permeability," in IEEE Transactions on Magnetics, vol. 61, no. 9, pp. 1-12, Sept. 2025.